

Research Article

Investigating the Combined Effects of Inherent and Stress-Induced Anisotropy on the Mechanical Behavior of Granular Materials Using Three-Dimensional Discrete Element Method

Xinran Chen, Jinsong Qian , Lei Zhang, and Jianming Ling

Key Laboratory of Road and Traffic Engineering of the Ministry of Education, Tongji University, 4800 Cao'an Road, Shanghai 201804, China

Correspondence should be addressed to Jinsong Qian; qianjs@tongji.edu.cn

Received 4 August 2020; Accepted 9 September 2020; Published 17 September 2020

Academic Editor: Bowen Guan

Copyright © 2020 Xinran Chen et al. This is an open access article distributed under the Creative Commons Attribution License, which permits unrestricted use, distribution, and reproduction in any medium, provided the original work is properly cited.

The three-dimensional discrete element method (DEM) was employed to investigate the combined effects of inherent and stress-induced anisotropy of granular materials. The particles were modeled following real particle shapes. Both isotropic and inherently anisotropic specimens were prepared, and then true triaxial numerical tests were conducted using different intermediate principle stress ratios (b). The results indicate that the oriented particles in the anisotropic specimens form strong contacts in their long axis direction in the early stages of shearing, which restrains the contraction of the specimens. As the strain increases, the oriented particles start to rotate and slide, which results in shorter contraction stages and fewer number of interparticle contacts with peak values compared to the isotropic specimens. In addition, the increase in b values aggravates the rotating and sliding of particles in the inherently anisotropic specimens and restrains the contraction of the granular and the increase of contact forces. As a result, the inherent anisotropy reduces the effects of stress-induced anisotropy on the mechanical behavior of granular materials.

1. Introduction

Granular materials are commonly used in the base layers of typical pavement structures. The directional distribution of particles in granular materials significantly affects their mechanical properties [1], which leads to an anisotropic phenomenon. The anisotropy of granular material can be divided into inherent anisotropy and stress-induced anisotropy [2]. Inherent anisotropy is induced by the directional arrangement of particles during compaction or deposition. Stress-induced anisotropy is caused by the nonuniform distribution of external loading, which leads to the rearrangement of the particles [3]. To investigate these two kinds of anisotropy, the long axis orientation (or “bedding angle”) of granular particles is widely used for inherent anisotropy analysis, and the intermediate principle stress ratio, denoted by b , which represents the relative magnitude of the intermediate principle stress, is used for stress-induced anisotropy analysis [4, 5].

Several researchers have conducted laboratory tests to study the effect of anisotropy on the mechanical responses of particle assemblies. For example, Guo [6] conducted direct shear tests using specimens with different bedding angles. The results showed that the friction angle of granular materials varies with the orientation of the shear plane relative to the bedding plane. Besides, the degree of anisotropy is affected by particle shapes. Shi et al. [7] investigated the effect of intermediate principle stress on the macroscopic mechanical responses of a coarse-grained soil using true triaxial tests. The results showed that shear strength and intermediate principle strain increase as the b value increases, whereas the minor principle strain decreases. However, some experimental studies have shown uncertain relationships among the angle of shear resistance, b values, and other controversial behavior [8, 9], as laboratory test results can be affected by the initial fabric difference [10, 11], different sample preparation methods [12, 13], different boundary conditions, etc. [14]. In recent years, researchers

used the discrete element method (DEM) [15] to investigate the behavior of granular materials from both macroscopic and microscopic perspectives [16, 17]. The DEM can simulate several test conditions using one specimen and thus avoid the initial fabric difference. Furthermore, microscopic characteristics at the particulate level are easy to obtain and can help to explain the stress and strain evolution during loading [18–20].

Several studies have been undertaken to investigate the anisotropy of soil and granular materials using the DEM. For example, Hosseininia [21] studied the inherent anisotropy of granular soils using a two-dimensional DEM and found that the initial distribution of elongated particles and associated voids vary during shear deformation. Besides, the shear strength and deformability of granular materials are highly dependent on the initial fabric condition. Barreto and O'Sullivan [22] studied the stress-induced anisotropy of soil under a constant mean load using a three-dimensional (3D) DEM. Results showed that the friction coefficient affects the inherent stability of the strong force chains, whereas the intermediate stress ratio affects the lateral support provided to these force chains. Kuhn et al. [23] conducted numerical simulations using a 3D DEM and described the anisotropy of the voids through image analysis and Minkowski tensors. Their results showed that stress-induced anisotropy affects not only the mechanical stress-strain relationship but also the hydraulic properties. Some studies that employed DEM also considered the complex stress path [5, 24] and particle breakage [25, 26]. However, related studies have focused mainly on the effect of different b values on isotropic samples; research into the behavior of inherently anisotropic granular materials under different b values is limited.

In real practice, the granular materials may be inherently anisotropic due to compaction or deposition, and may also work under complex stress states that cause stress-induced anisotropy. Therefore, the combined effects of the two types of anisotropy may affect the mechanical behavior of granular materials simultaneously and thus needs further investigations.

For this purpose, 3D DEM simulations were conducted for this study. Isotropic and inherently anisotropic granular specimens were prepared, and then true triaxial numerical tests were conducted using different b values. Finally, the macroscopic and microscopic responses, including stress-strain characteristics, interparticle contacts, and the anisotropies of contact normal and contact force, were analyzed in detail to address the mechanisms of anisotropy.

2. Numerical Model

2.1. Particle Modeling and Grading. In DEM simulations, the particle shape can obviously affect the anisotropic properties [3, 6, 27, 28]. Although the use of circular discs (in 2D) or spheres (in 3D) can significantly reduce the calculation time, they can also lead to excessive freedom of the particles and thus a higher degree of rotation and dilation compared with real granular particles [21, 29–31]. Therefore, noncircular/nonspherical particles are widely used and typically are oval or spherical particles made by clusters of bonded circles/

spheres or overlapping rigid clusters [29, 32, 33]. Some researchers have tried another approach that uses convex polygon-shaped particles [34, 35]. The simulation accuracy and computational efficiency of these approaches are of vital importance and are a primary focus of related research.

In this study, the numerical simulations utilized 3D DEM software, Itasca PFC^{3D} (version 5.0). Ten typical shapes of granular particles were considered in the DEM simulations and were modeled in 3D following real particle shapes, as shown in Figure 1(a). Then, based on the bubble pack algorithm proposed by Taghavi [36], the 3D models were filled with different sized balls which partially overlapped each other without generating force to create complex clumps in PFC^{3D}. During the filling process, the largest ball was placed first, followed by decreasingly smaller balls. The distance parameter, which controls the overlap of adjacent balls, and the ratio parameter, which is the ratio of the smallest to the largest ball, both affected the simulation accuracy and calculation efficiency. After several pretests, the distance and ratio parameters were set at 100 and 0.3, respectively. Figure 1(b) presents a comparison of a real particle, the original 3D model, and the PFC^{3D} particle.

In order to simulate an actual granular base that consists of particles of different sizes, a widely used grade was selected for the DEM simulations [31, 37]. In accordance with previous research studies, fine particles were deleted and the particle sizes were adjusted to consider computational efficiency [38, 39], as shown in Figure 2. It should be noted that, the DEM specimen without fine-graded particles may be less dense and more compressible than actual granular material [40]. This simplification would affect the values of some macro-microindexes, but the comparison among different anisotropic conditions would be less affected.

The total number of particles used for the numerical specimens were calculated using the target porosity of 0.33. To avoid the size effect, previous studies suggest that the diameter of the specimen should be at least 10 times larger than the maximum particle size [38, 41]. Therefore, the dimensions of each granular specimen were set to $15^L \times 15^W \times 15^H \text{ cm}^3$, and 6,884 particles were used. The ten different particle shapes were randomly distributed. Table 1 lists both the particle sizes and numbers of particles used in this study.

2.2. Specimen Preparation. Two specimen types were used in DEM simulation, which are the isotropic specimens and inherently anisotropic specimens. Both types of specimens were prepared using the gravitational deposition method [42, 43]. First, a deposition space of $15^L \times 15^W \times 30^H \text{ cm}^3$ was created and enclosed by six frictionless rigid walls, and the particles were then generated in the space, as shown in Figure 3. For the isotropic specimens, the long axis of the particles was randomly distributed, whereas for the inherently anisotropic specimens, the long axis of the particles was arranged in the intermediate principle stress (σ_2) direction. During specimen preparation, the particle rotation was fixed to obtain the anticipated anisotropic conditions. Then, the gravity field was introduced using the gravitational forces

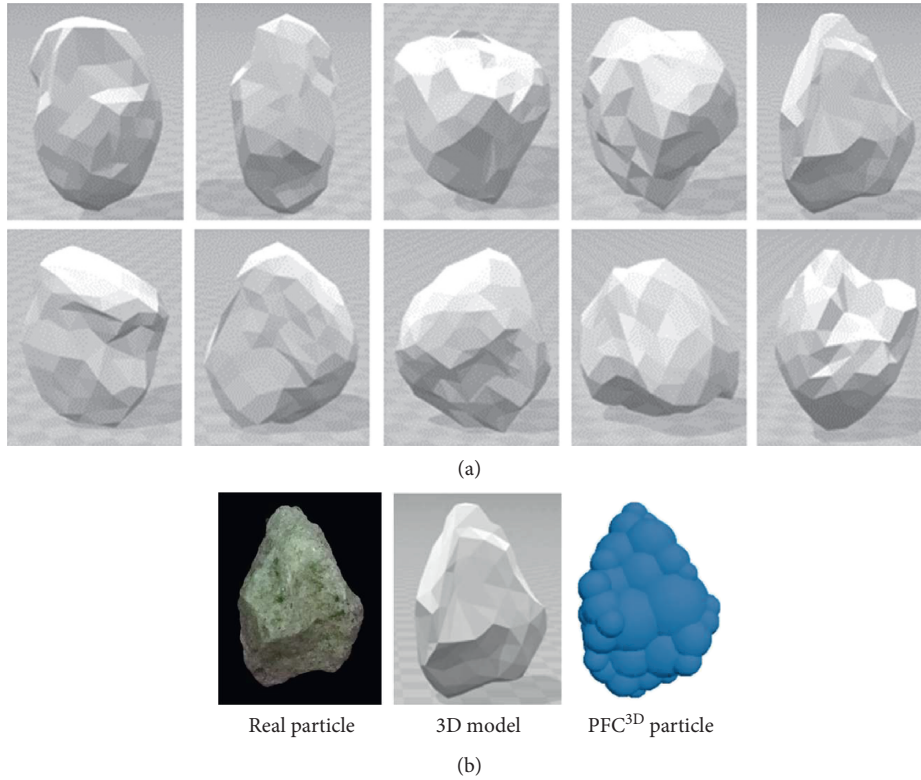


FIGURE 1: (a) 3D granular models of different particle shapes and (b) comparison of the real particle, 3D model, and PFC3D particle.

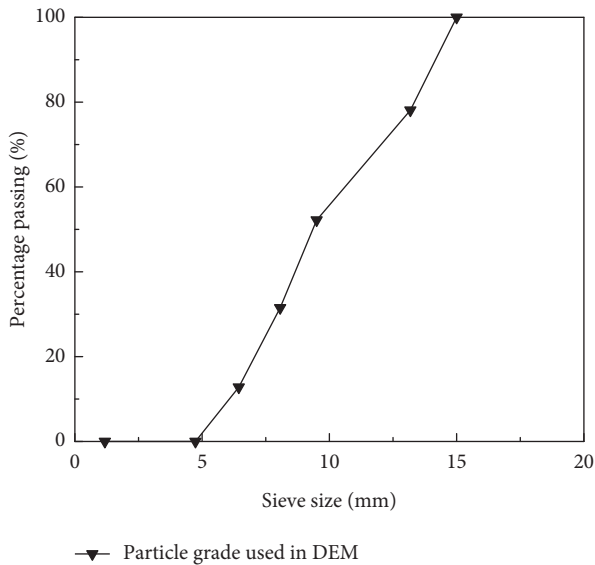


FIGURE 2: Particle size distribution curve used in the DEM simulation.

applied to all particles in the vertical direction; thus, the particles would be deposited on the bottom boundary of the deposition space. To create a dense specimen and reduce the simulation time during specimen preparation, the particle friction coefficient was temporarily set as zero [5, 29]. At the end of the deposition, a space of $15^L \times 15^W \times 15^H \text{ cm}^3$ was chosen as the final specimen size. Finally, the specimen was

TABLE 1: Particle size and number of particles for different specimens.

Particle size (mm)	4.75–6.5	6.5–8	8–9.5	9.5–13.25	13.25–15
Number of particles	3925	1346	878	531	204

isotropically compressed by giving the same loading speed to all six rigid walls until the target confining pressure of 100 kPa was reached. Figure 3(e) presents the isotropic and anisotropic specimens after preparation.

The linear contact model [44] was adopted to simulate the interparticle contacts for computational efficiency. In accordance with related studies which also studied the mechanical behavior of granular materials [30, 39, 45, 46], the material parameters were selected for triaxial testing. The stiffness ratio κ^* , effective modulus E^* friction coefficient μ , damping constant, and particle density were set at 1.333, $1 \times 10^8 \text{ Pa}$, 0.5, 0.7, and 2.6 g/cm^3 , respectively.

2.3. True Triaxial Shearing. The true triaxial tests were conducted using a strain-controlled loading process that was performed by moving the rigid walls of the specimens. As suggested by Andrade et al. [47], increased loading speed increased the calculation efficiency but would affect the mechanical behavior of granular materials due to the dynamic effect. To select a proper loading speed, a sensitivity analysis was conducted using isotropic specimens under five loading speeds ranged from 0.03 m/s to 0.50 m/s, as depicted

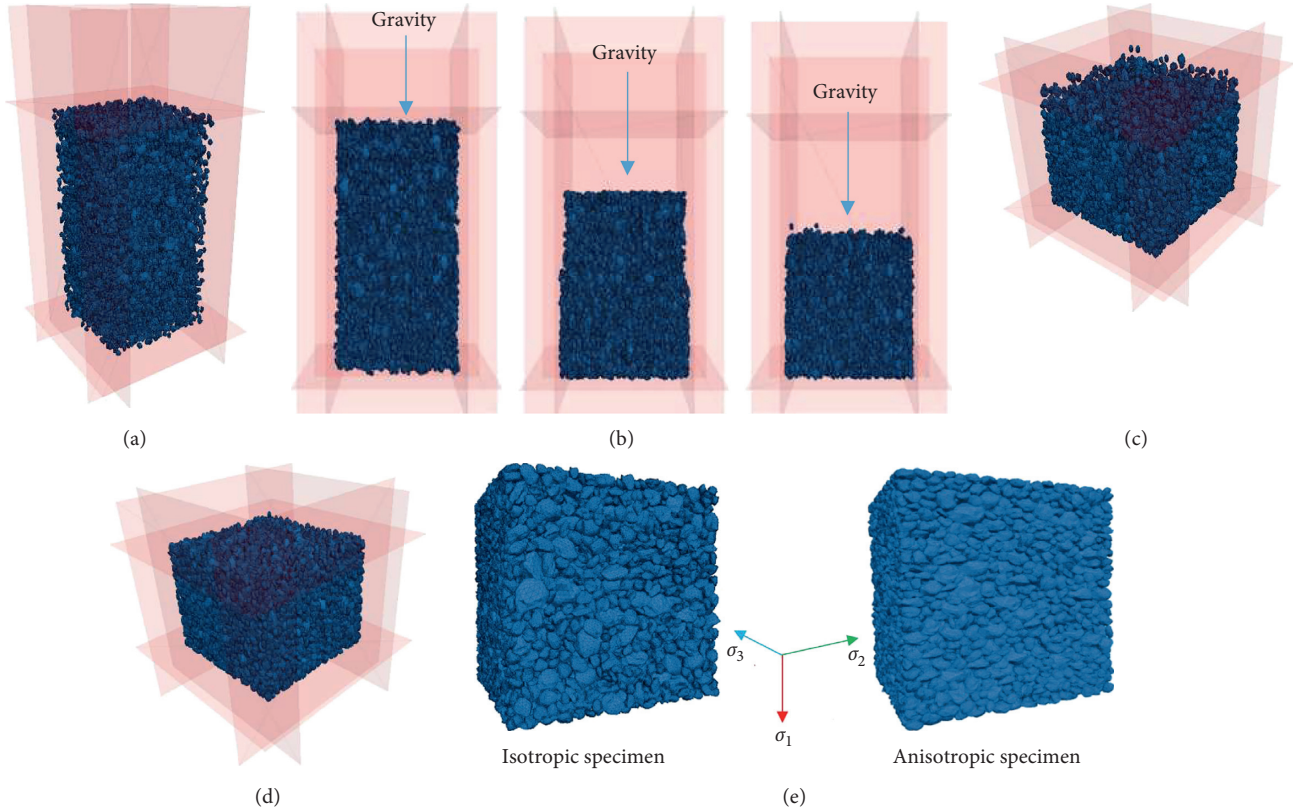


FIGURE 3: The procedure of specimen preparation: (a) particles' generation; (b) gravitational deposition; (c) resizing the walls; (d) isotropic compression; (e) specimens after preparation.

in Figure 4. It can be seen that the porosity, which reflects the volume change of the specimens, changes obviously under high loading speeds. By contrast, the porosity is similar for selected small loading speeds. This indicates that the loading speed had a threshold between quasi-static and dynamic. Thus, the loading speed for this study was set at 0.12 m/s to ensure the loading process was quasi-static.

To simulate stress-induced anisotropy, the intermediate principle stress ratio, b , was induced and is defined as

$$b = \frac{(\sigma_2 - \sigma_3)}{(\sigma_1 - \sigma_3)}, \quad (1)$$

where σ_i ($i = 1, 2, 3$) are the principle stresses. In this paper, the stress and strain indexes take positive values when the granular is compressed.

Five b values ($b = 0.00, 0.25, 0.50, 0.75, 1.00$) were selected for the numerical tests. The test under $b = 0.00$ ($\sigma_2 = \sigma_3$) represents the triaxial compression test, and the test under $b = 1.00$ ($\sigma_1 = \sigma_2$) is the triaxial extension test. The major principle stress σ_1 changes when the top wall moves during testing, so the intermediate principle stress can be calculated using the following equation:

$$\sigma_2 = b(\sigma_1 - \sigma_3) - \sigma_3. \quad (2)$$

The minor principle stress σ_3 was set at 100 kPa for all conditions, and b values were also kept constant during the numerical simulation, so the relationship between σ_1 and σ_2

could be expressed by $d\sigma_2 = bd\sigma_1$. During triaxial shearing, the σ_2 was dynamically adjusted by stress servo-control method to keep equation (2) satisfied.

2.4. Verification of the DEM Simulation. The DEM model was verified by the true triaxial test results conducted by Shi [48]. For the laboratory test, the fine gravel was used with the particle diameter ranged from 2–5 mm. The diameter of the laboratory test specimen is 70 mm × 35 mm × 70 mm, and the loading conditions are the same as the DEM simulation. The long axis of the particles in the laboratory test was randomly distributed, which consists of the isotropic DEM specimen.

The comparison between the laboratory test and the numerical simulation results is depicted in Figure 5. It can be seen that the stress-strain relationship and the peak stress ratio obtained from DEM simulation and laboratory test share the same trend, and the values are similar to each other. Therefore, it can be indicated that the DEM model is reasonable.

3. Numerical Simulation Results

3.1. Macroscopic Analysis: Stress-Strain Characteristics. To evaluate the stress-strain characteristics of granular materials with different initial fabrics and under different b values, several commonly used macroscopic indexes are

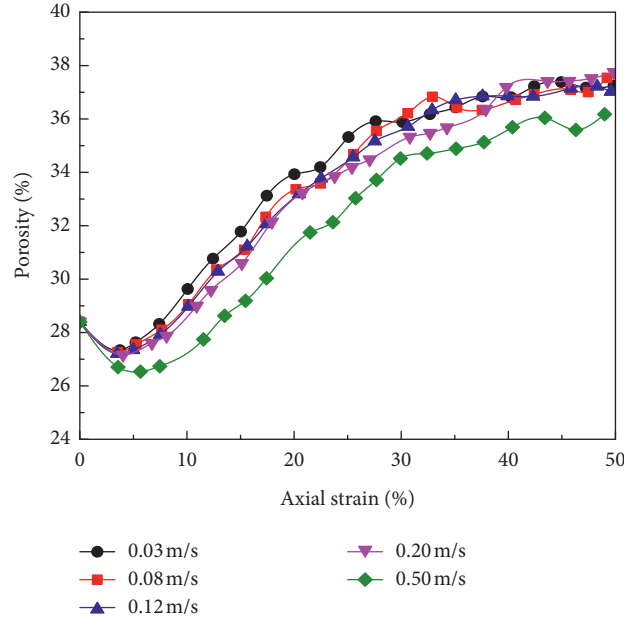


FIGURE 4: The effect of the loading speed sensitivity on the porosity.

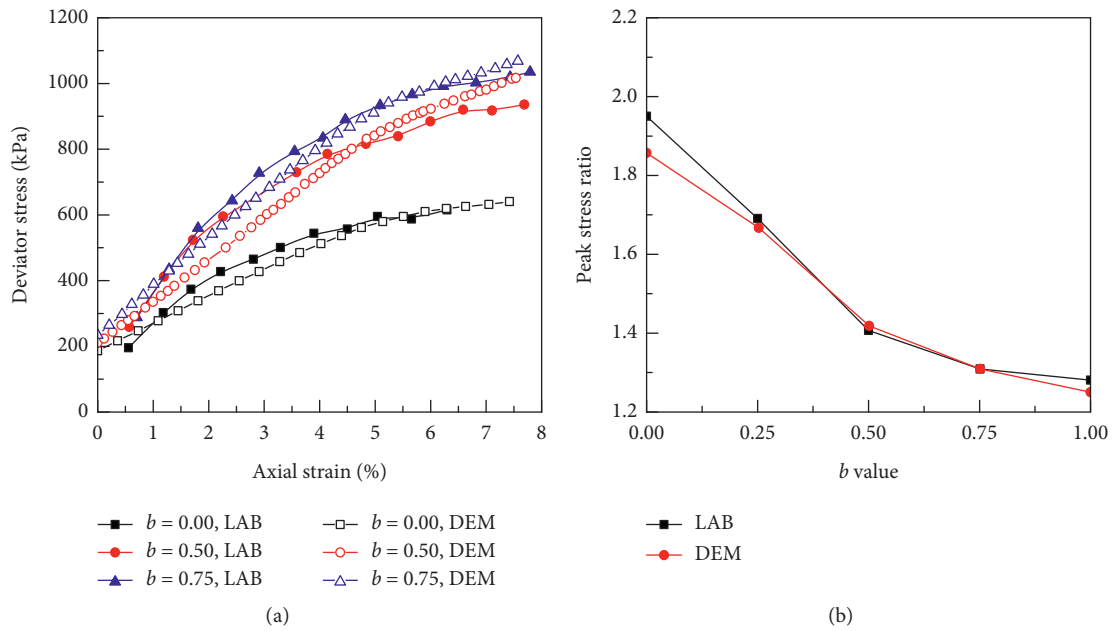


FIGURE 5: Comparison between the DEM model and laboratory tests: (a) the deviator stress; (b) the peak stress ratio.

selected based on the stress and strain in three principle stress directions. The peak internal friction angle (φ_{\max}), mean stress (p), shear stress (q), major principle strain (ε_1), and volumetric strain (ε_v) are defined, respectively, as equation (3)–(7) [49]:

$$\sin \varphi_{\max} = \frac{(\sigma_1/\sigma_3)_{\max} - 1}{(\sigma_1/\sigma_3)_{\max} + 1}, \tag{3}$$

$$p = \frac{(\sigma_1 + \sigma_2 + \sigma_3)}{3}, \tag{4}$$

$$q = \sqrt{\left(\frac{1}{2}\right) [(\sigma_1 - \sigma_2)^2 + (\sigma_2 - \sigma_3)^2 + (\sigma_1 - \sigma_3)^2]}, \quad (5)$$

$$\varepsilon_1 = \ln\left(\frac{H_0}{H}\right), \quad (6)$$

$$\varepsilon_v = \ln\left(\frac{V}{V_0}\right), \quad (7)$$

where H_0 and V_0 are the initial height and volume of the specimen, respectively, and H and V represent the height and volume of the specimen at time t , respectively.

The relationship between φ_{\max} and b value is commonly used to investigate of peak strength in true triaxial testing. Figure 6(a) shows that, for both specimen types, φ_{\max} increases as the b value increases from 0.00 to 0.75 and then decreases as the b value increases from 0.75 to 1.00. Similar trend was also found by previous studies using laboratory tests [47, 49] and DEM simulations [4, 5, 11]. The peak value of the mean stress (p_{\max}) that represents the overall stress level increases as the b value increases for both specimen types, as shown in Figure 6(b). Because all the numerical tests were conducted using the same σ_3 value, the σ_2 value increases as the b value increases and leads to the increase in the mean stress.

Compared to the isotropic specimens, the φ_{\max} and p_{\max} values for anisotropic specimens are lower at the same b values and change less as the b value increases. This finding indicates that the horizontal alignment of the long axis of the particles reduces the effect of nonuniform stress distribution on the stress behavior of granular materials.

To highlight the effects of the nonuniform distribution of external loading on the stress behavior of the granular materials, the stress ratio, defined as q/p , is introduced. Figure 7 shows that, for the isotropic specimens, the stress ratio decreases as the b value increases, which is consistent with related laboratory test results [50] and numerical simulation results [4, 14]. Also, the stress ratios for both specimen types are similar at the same b values. This finding indicates that the increased proportion of σ_2 results in the decrease of the shear strength of granular materials, and this effect is similar for both isotropic and inherently anisotropic granular specimens.

Figure 8 shows the variation of (ε_v) with the major principle strain ε_1 . All specimens exhibit the process from contraction to dilation as ε_1 value increases. For the isotropic specimens, the amount of contraction tends to increase as the b value increases. By contrast, the anisotropic specimens are less contracted than the isotropic specimens for all the selected b values, and their contraction stages end with smaller ε_1 values. This finding indicates that the inherently anisotropic granular materials are less compressible and may dilate earlier than isotropic granular materials and that the effect of b values on strain behavior is reduced.

3.2. Microscopic Analysis: Contact Characteristics. In order to illustrate the macroscopic behavior of granular materials at the particle scale, the contact characteristics are analyzed.

The coordination number (CN) is a commonly used index that is directly related to the stability of granular material [4, 51] and is defined as the average number of contacts per particle:

$$\text{CN} = \left(\frac{2N_c - N_c^w}{N_p}\right), \quad (8)$$

where CN is the coordination number, N_c is the total number of contacts, N_c^w is the number of contacts between the particle and the wall, and N_p is the total number of particles.

Figure 9 shows the evolution of the CN with the major principle strain. For both specimen types, the CN increases with ε_1 to the peak value and then decreases to a residual value. The peak CNs increase obviously as the b value increases. Compared to the isotropic specimens, the inherently anisotropic specimens have higher initial CNs, lower peak CNs, and smaller ε_1 values that correspond to the peak CNs. Besides, the increase of their peak CNs as b value increases is much smaller than isotropic specimens. This finding indicates that the oriented arrangement of particles in inherently anisotropic specimens form more contacts in the early stage of shearing, and the change of CNs during shearing is less affected by nonuniform stress distribution.

During triaxial testing, the contact sliding typically occurs during the rearrangement of the particles, thus resulting in the permanent deformation of the granular materials. As defined by Gu et al. [39], contact slides when the inequality, shown as equation (9), is satisfied:

$$\frac{|f^t|}{(\mu f^n)} > 0.9999, \quad (9)$$

where f^n and f^t are the normal contact force and tangential contact force, respectively, and μ is the contact friction coefficient.

Figure 10 presents a comparison of the initial and peak sliding contact percentages during triaxial shearing for all specimens. For both specimen types, the initial sliding contact percentages increase as b value increases from 0.00 to 0.25, and decrease as b value increases from 0.25 to 1.00. The peak sliding contact percentages for the isotropic specimens decrease as the b value increases, which is consistent with the DEM simulation results of Mahmud Sazzad et al. [4]. By contrast, the peak sliding contact percentages for the anisotropic specimens decrease as the b value increases from 0.00 to 0.75, then tend to increase as the b value increases from 0.75 to 1.00. Under the same b values, the anisotropic specimens have lower initial sliding contact percentages and higher peak sliding contact percentages compared to the isotropic specimens. This finding indicates that the sliding of contacts is restrained as the b values increase for isotropic specimens. By contrast, the anisotropic specimens restrain contact sliding in the early stages of testing compared with isotropic specimens, but contact sliding occurs more during shearing, especially with high b values.

Both the CNs and the sliding contact percentages can be used to explain the change of volumetric strain (see

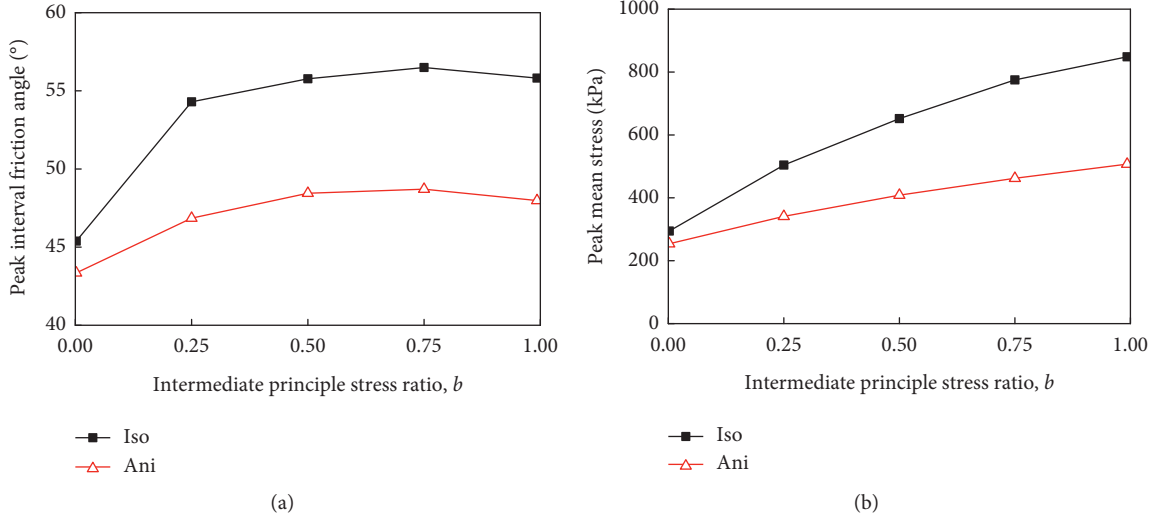
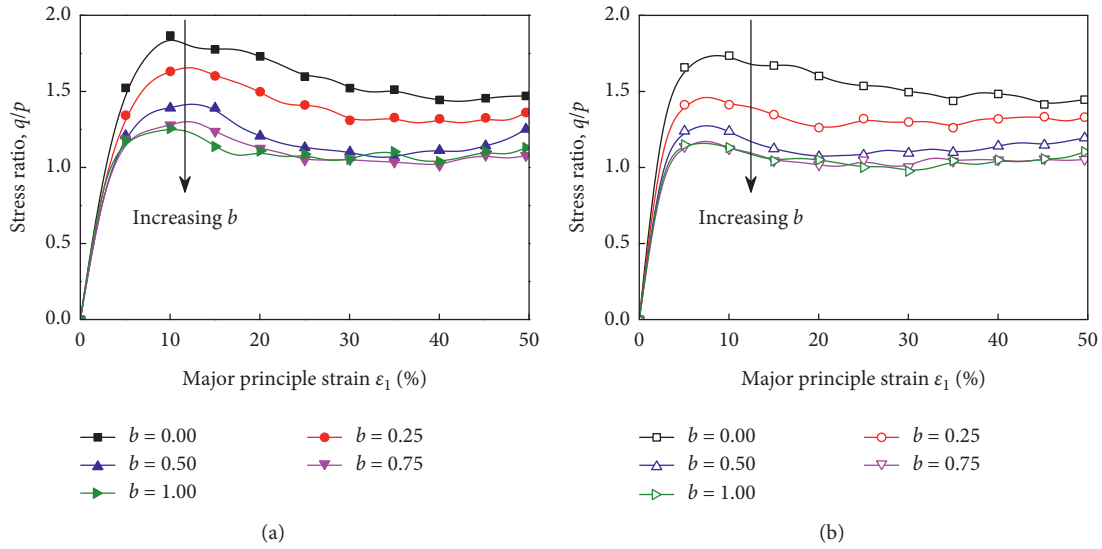

 FIGURE 6: Comparison of (a) peak internal friction angle (φ_{\max}) and (b) peak mean stress (p_{\max}).

 FIGURE 7: Evolution of stress ratio with the increase of ε_1 : (a) isotropic specimens; (b) anisotropic specimens.

Figure 8). During the contraction stage, the particles are squeezed together in close contact with each other, which leads to an increase in the CN value. During the dilation stage, the particles start to rotate and slide, which results in the decrease of CN [51]. The specimen which is contracted mostly also has the largest peak CN and the lowest peak sliding contact percentage.

3.3. Microscopic Analysis: Fabric Tensor and Anisotropy. The directional distribution of particles, defined as the fabric, plays an important role in the shear behavior of a particle assembly [52–55]. To further investigate the combined effects of inherent and stress-induced anisotropy of granular materials, the contact normal, normal contact force, and tangential contact force are induced.

The directional distribution of the contact normal is usually described by the fabric tensor R_{ij} [56, 57]:

$$R_{ij} = \int_{\Omega} E(\Omega) n_i n_j d\Omega = \left(\frac{1}{N} \right) \sum_{c \in N} n_i n_j, \quad (10)$$

where n_i is the unit contact normal in the i -direction, N is the total number of contacts, and $E(\Omega)$ is the distribution function on the unit sphere Ω and can be calculated by the second-order Fourier expansion as follows [58]:

$$E(\Omega) = \left(\frac{1}{4\pi} \right) [1 + \alpha_{ij}^r n_i n_j], \quad (11)$$

where α_{ij}^r is the second-order anisotropic tensor and characterizes the fabric anisotropy. This tensor is determined by the deviatoric part of the fabric tensor (R_{ij}^d) as

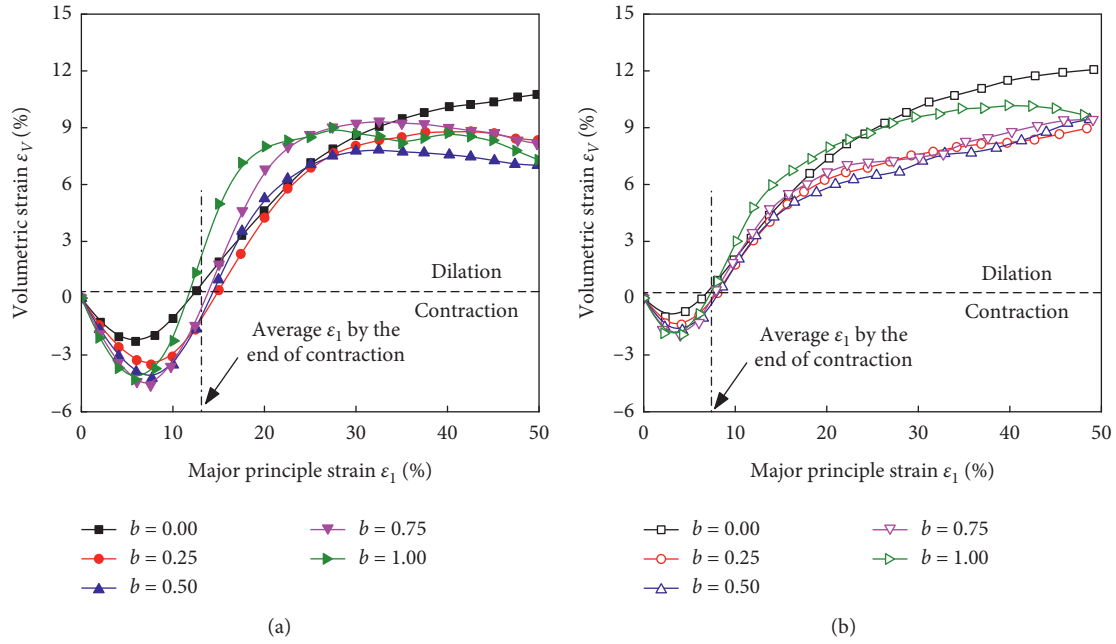


FIGURE 8: Variation of volumetric strain with the increase of ε_1 : (a) isotropic specimens; (b) anisotropic specimens.

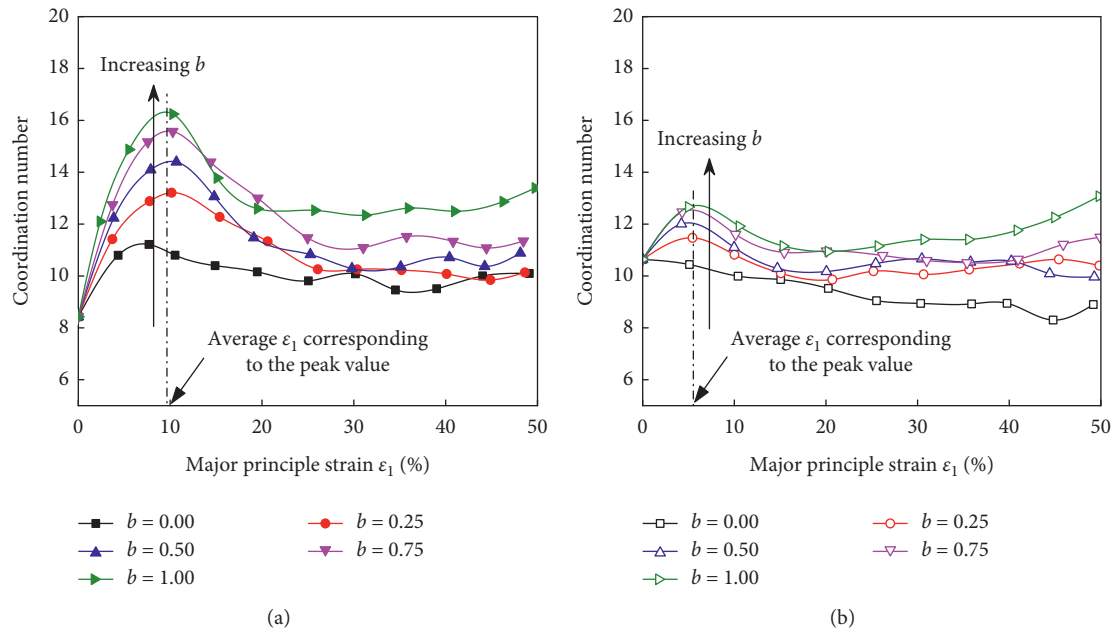


FIGURE 9: Evolution of coordination number with the increase of ε_1 : (a) isotropic specimens; (b) anisotropic specimens.

$$\alpha_{ij}^r = \left(\frac{15}{2}\right) R_{ij}^r. \quad (12)$$

For normal and tangential contact force, the similar definition is induced, as expressed in equation (13)–(18):

$$F_{ij}^n = \left(\frac{1}{4\pi}\right) \int_{\Omega} \bar{f}^n(\Omega) n_i n_j d\Omega = \sum_{c \in N} \frac{f^n n_i n_j}{N(1 + \alpha_{kl}^r n_k n_l)}, \quad (13)$$

$$\bar{f}^n(\Omega) = \bar{f}_0^n (1 + \alpha_{ij}^n n_i n_j), \quad (14)$$

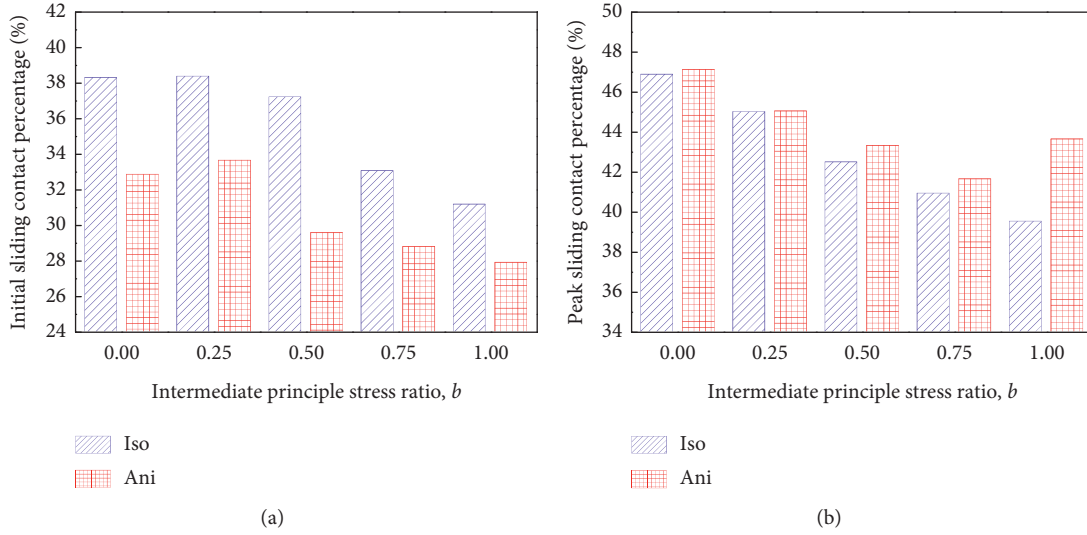


FIGURE 10: Comparison of (a) initial sliding contact percentages and (b) peak sliding contact percentages.

$$\alpha_{ij}^n = \left(\frac{15}{2}\right) \left(\frac{F_{ij}^{n'}}{\bar{f}_0^n}\right), \quad (15)$$

$$F_{ij}^t = \left(\frac{1}{4\pi}\right) \int_{\Omega} \bar{f}_i^t(\Omega) n_i n_j d\Omega = \sum_{c \in N} \frac{f^t n_i n_j}{N(1 + \alpha_{kl}^r n_k n_l)}, \quad (16)$$

$$\bar{f}_i^t(\Omega) = \bar{f}_0^n [\alpha_{ij}^t n_j - (\alpha_{kl}^t n_k n_l) n_i], \quad (17)$$

$$\alpha_{ij}^t = \left(\frac{5F_{ij}^t}{\bar{f}_0^n}\right), \quad (18)$$

where f^n is the normal contact force, f^t is the tangential contact force, and \bar{f}_0^n is the average normal contact force over all the groups on Ω .

Note that α_{ij}^r , α_{ij}^n , and α_{ij}^t are symmetric and deviatoric, so their second invariants α_r , α_n , and α_t are used to quantify the degree of anisotropy as

$$\alpha_* = \sqrt{\left(\frac{3}{2}\right) \alpha_{ij}^* \alpha_{ij}^*}, \quad (19)$$

where the super and subscript * represents the contact normal r , tangential contact force t , and normal contact force n , respectively.

Figure 11 shows that the α_r , α_n , and α_t values increase at the beginning and then decrease to a residual value as ε_1 value increases. As the b value increases, the initial slope of α_r , shows a small difference, whereas the peak values and residual values decrease obviously. This finding indicates that the contact distribution tends to be more uniform with a higher b value. Besides, the α_n values are about 3 to 4 times higher than the α_t values for all conditions, which suggests that contact force anisotropy is mainly caused by normal contact forces [51].

The initial α_r values for the two specimen types are significantly different. The isotropic specimens have an

initial α_r at zero, which means the initial contact distribution is uniform. By contrast, the anisotropic specimens have an initial α_r , at about 1.0, which means the oriented arrangement of particles make the initial contact distribution nonuniform. However, the peak and residual α_r values for two specimen types are similar, which suggests that inherent anisotropy changes the initial contact distribution, but will not obviously affect the extent of contact normal anisotropy during shearing. For α_n and α_t , the values change with different b values for anisotropic specimens is smaller than the isotropic specimens, which suggests that inherent anisotropy significantly reduces the effect of b values on the distribution of contact force of granular materials.

To address the reason for the difference in anisotropy parameters α_r and α_n , between the two specimen types, the principle values corresponding to them are induced. The α_t is not analyzed here because it is much smaller than α_n .

The principle values of the fabric tensor R are used to quantify the cluster extent of contacts in the principle stress directions [14]. R_1 , R_2 , and R_3 represent the contact clustering extent in the σ_1 , σ_2 , and σ_3 direction, respectively. As shown in Figure 12, the R principle values show similar trends with the increase of ε_1 for both specimen types. Before the peak of R principle values, R_1 increases, whereas R_3 decreases as ε_1 value increases for all the selected b values. R_2 decreases with the increase of ε_1 when $b < 0.5$ and increases as ε_1 value increases when $b > 0.5$. Such trends are similar to the precious DEM simulation results [11, 14, 22], which also indicates that contacts tend to cluster in the σ_1 direction to carry most of the external load. As the b value increases, the contacts also cluster in the σ_2 direction.

The anisotropic specimens have higher R_3 values and lower R_2 values compared with the isotropic specimens for all selected b values; thus, the contact normal anisotropy α_r for the two specimen types is similar. In addition, for the anisotropic specimens, the R_2 value is lower than the R_3 value under selected small b values, whereas for the isotropic specimens, the relationship is opposite. This finding

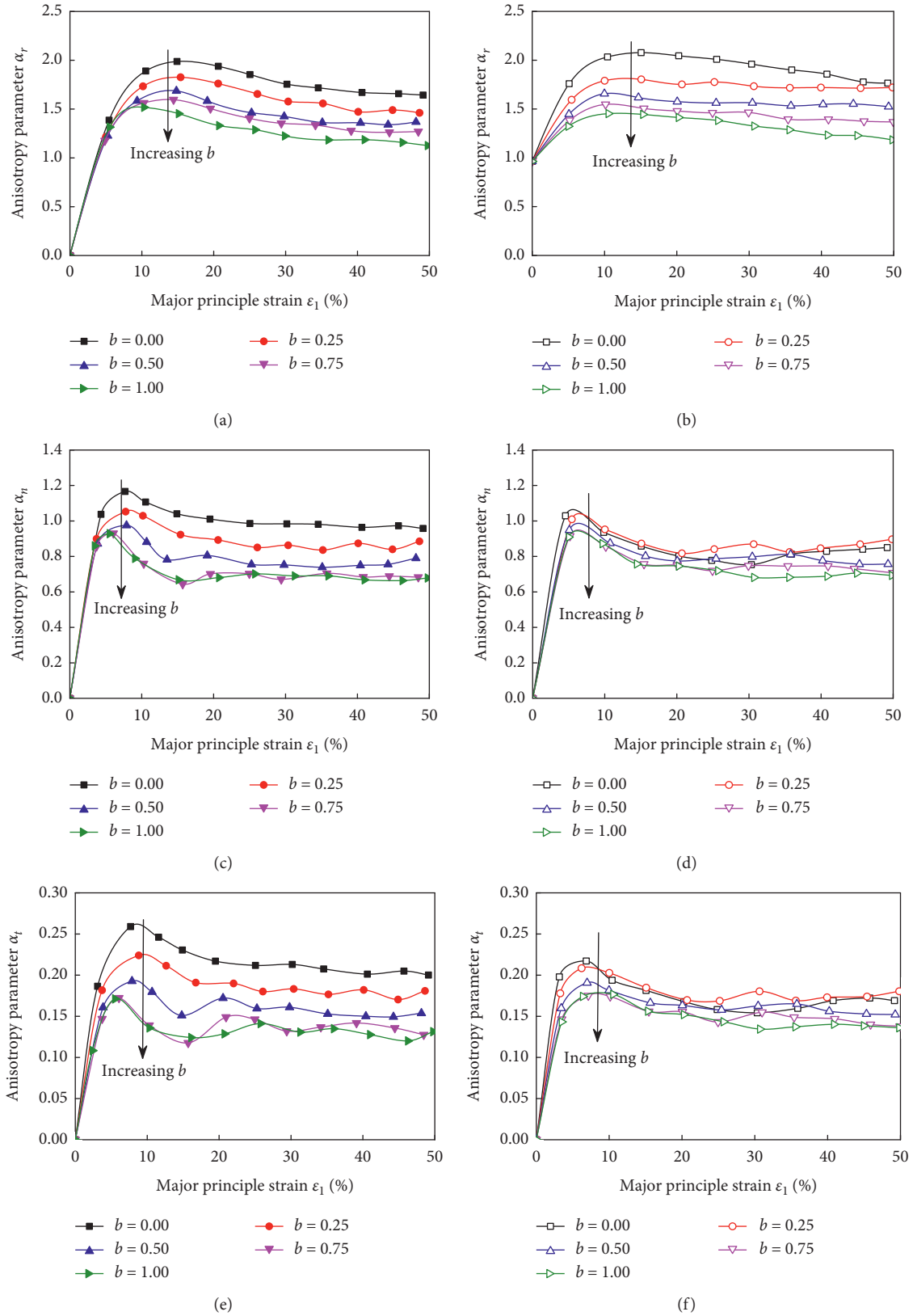


FIGURE 11: Effects of b values on the anisotropy parameter α_r , α_n , and α_t . (a) α_r Iso, (b) α_r Ani, (c) α_n Iso, (d) α_n Ani, (e) α_t Iso, and (f) α_t Ani.

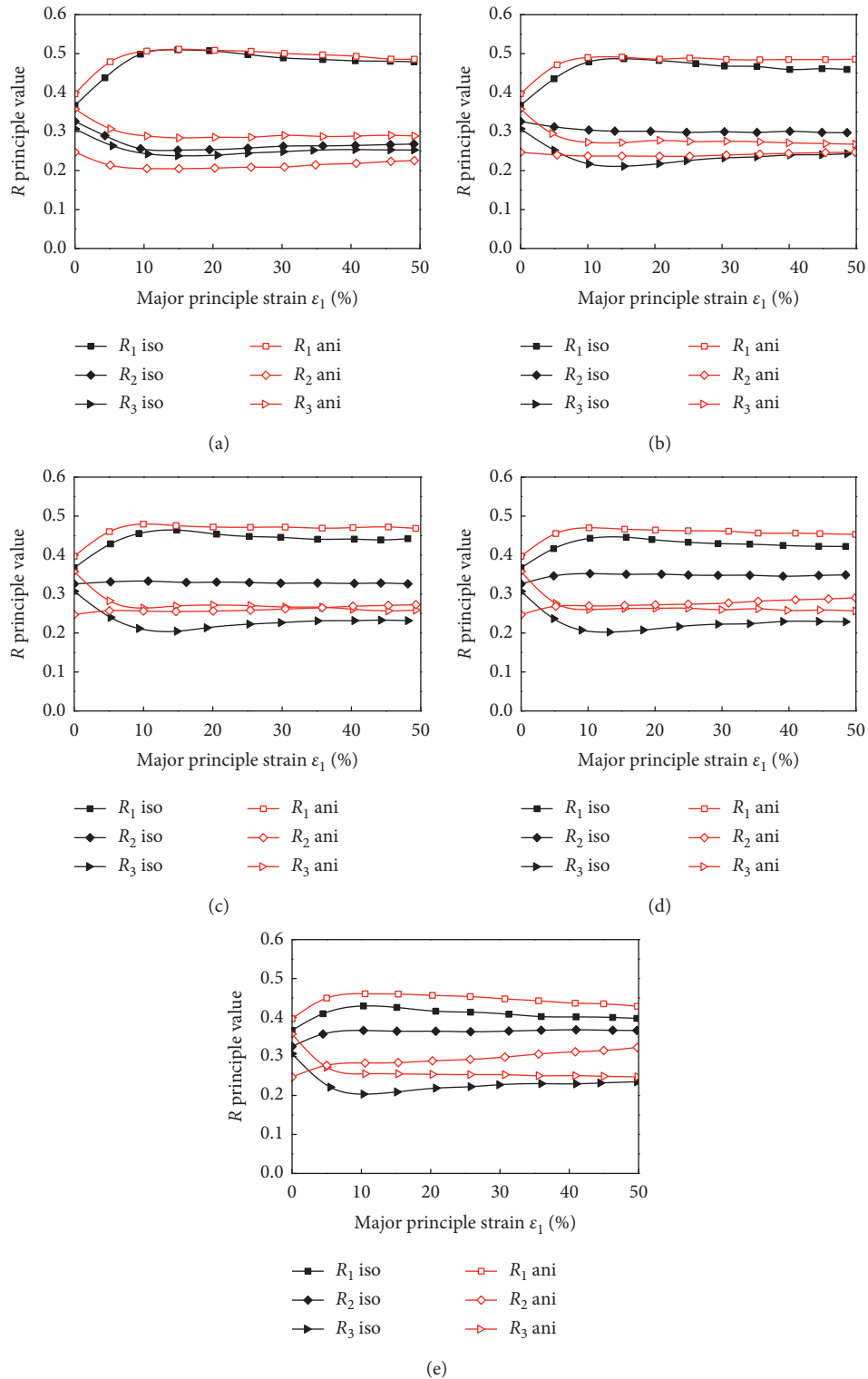


FIGURE 12: Evolution of the R principle values with an increase in b values: (a) $b = 0.00$; (b) $b = 0.25$; (c) $b = 0.50$; (d) $b = 0.75$; (e) $b = 1.00$.

indicates that the inherently anisotropic specimens form less contact in the direction of the long axis orientation of particles during shearing, compared with isotropic specimens.

Figure 13 shows the principle values of the normal contact force tensor F_n (F_{n1} , F_{n2} , F_{n3}). The trends

are similar for the three F_n principle changes as the ϵ_1 increases. As b value increases, all three F_n principle values increase obviously, which leads to the increase of peak internal friction angle and peak mean stress (Figure 6).

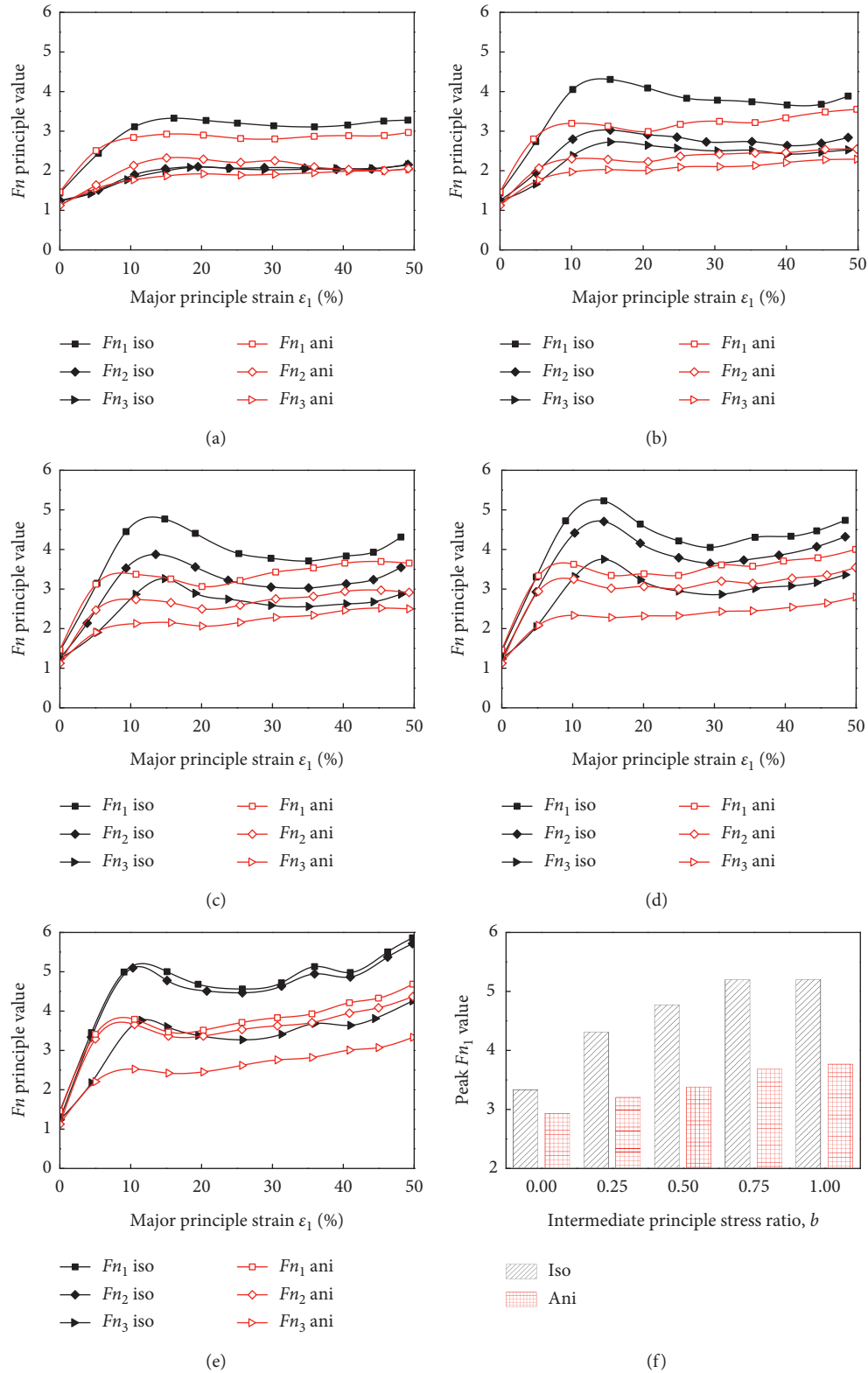


FIGURE 13: Evolution of the F_n principle values with the increase in b values: (a) $b = 0.00$; (b) $b = 0.25$; (c) $b = 0.50$; (d) $b = 0.75$; (e) $b = 1.00$; (f) comparison of peak F_{n1} values.

Compared to the isotropic specimens, the anisotropic specimens have lower principle F_n values (except for F_{n2} when $b = 0$), and the growth rate of contact force for

anisotropic specimens is lower as the b value increases, as shown in Figure 13(f). Therefore, the difference in α_n for the anisotropic specimens among different b values is smaller

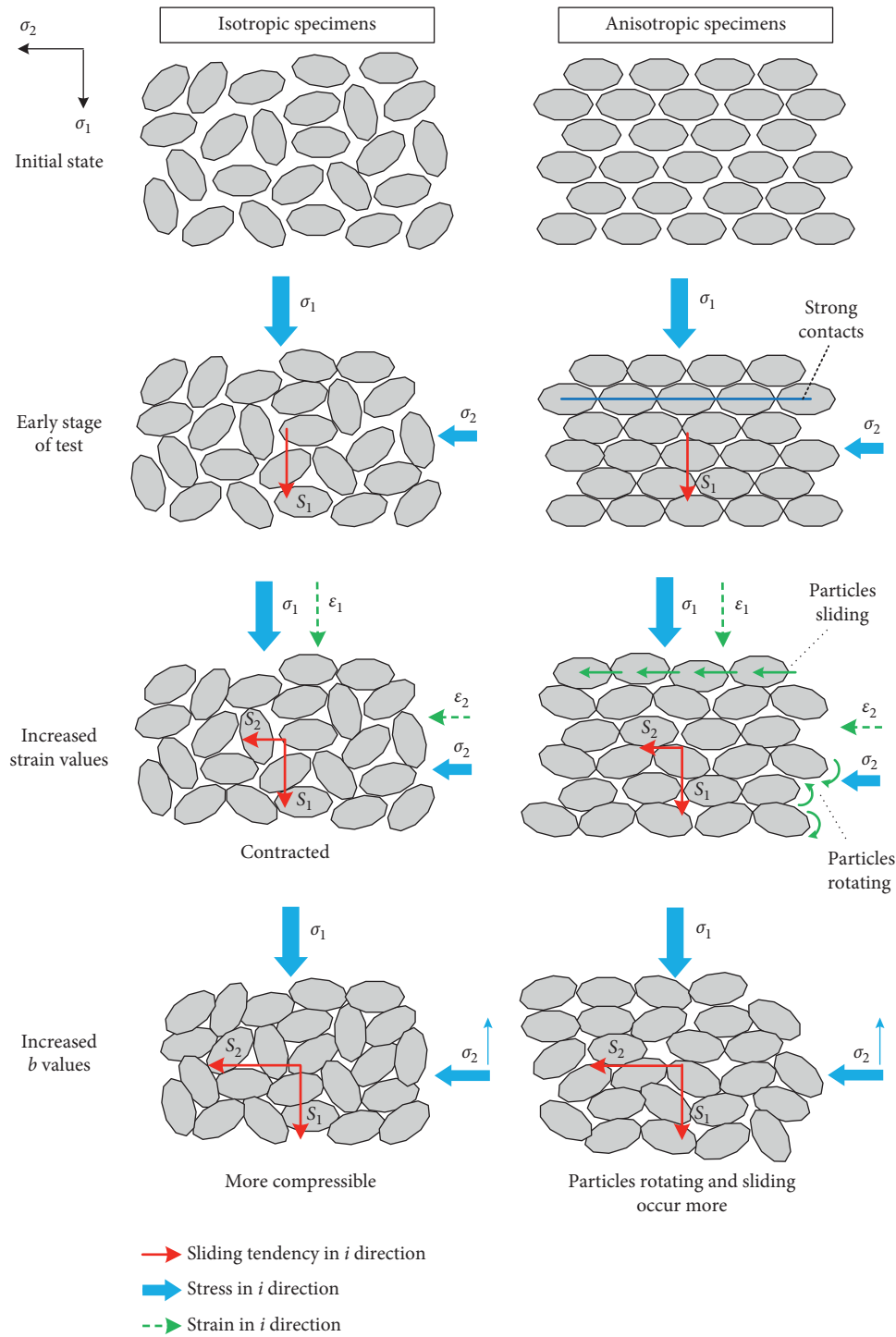


FIGURE 14: Schematics of the combined effects of inherent and stress-induced anisotropy.

(Figure 11), and their peak internal friction angle and peak mean stress are lower than isotropic specimens (Figure 6).

For the anisotropic specimens, the clustering of the contact normal in the σ_2 direction (R_2) is lower than in the σ_3 direction (R_3) for the selected small b values (Figure 12), whereas the clustering of the contact force in the σ_2 direction (Fn_2) is higher than the σ_3 direction (Fn_3), which suggests that the oriented particles form strong contacts in their long

axis direction and thus comprise of a strong force subnetwork [51, 56, 59, 60].

3.4. Discussion of the Combined Effects of Anisotropy. In summary, the combined effects of inherent anisotropy and stress-induced anisotropy can be illustrated in Figure 14. For selected small b values, the long axis of the particles in the

anisotropic specimens are initially perpendicular to the σ_1 direction to carry most of the external load [21] and resist the sliding tendency in σ_1 direction. Also, these particles form strong contacts in the σ_2 direction, as explained in Section 3.3. Therefore, the anisotropic specimens form a support frame in the early stages of testing, which leads to higher initial CN values and lower initial sliding contact percentages and makes the specimens less compressible compared with isotropic specimens. As the strain value increases, the isotropic specimens are obviously compressed, whereas for the anisotropic specimens, particle rotating and sliding occur due to the increased deformation in the σ_2 direction, which leads to higher peak sliding contact percentages, restrains the increase in the CNs, and shortens the contraction stage.

The increase in b values increases the proportion of σ_2 , thus leads to a greater sliding tendency in σ_2 direction. For isotropic specimens, the increase in b values leads to higher peak CNs, restrains the sliding of the contacts, and thus makes the specimens more compressible. For inherently anisotropic specimens, the increased b value significantly aggravates the rotating and sliding of the oriented particles and offsets its compressive effect. Therefore, the anisotropic specimens have higher peak sliding contact percentages and lower growth rate for the coordination number and contact force and are less compressible than the isotropic specimens. As a result, the effect of b values on the mechanical behavior of anisotropic specimens is significantly reduced when combined with the inherently anisotropic condition, compared with isotropic specimens.

4. Conclusion

This paper discussed the results of numerical simulations to investigate the combined effects of inherent and stress-induced anisotropy on the mechanical behavior of granular materials using 3D DEM. The macroscopic stress-strain relationships, microscopic contact characteristics, and anisotropic parameters were analyzed in detail and could be used to provide insights into the mechanism of anisotropy. The following conclusions can be drawn from this study:

- (i) The macroscopic and microscopic responses of granular materials are significantly affected by b values. The increase in b values makes isotropic specimens more compressible and leads to lower shear strength at the same stress level, and the directional distribution of contact normal and contact force becomes more uniform.
- (ii) Compared with isotropic specimens, the oriented granular particles in inherently anisotropic specimens form a support frame in the early stages of triaxial shearing, and thus make the granular material less compressible. As the strain increases, the oriented particles start to rotate and slide, which result in the redistribution of interparticle contacts and make the granular tend to dilate.
- (iii) When applying on the inherently anisotropic specimens, increased b values break the strong

contacts parallel to the long axis of particles, aggravate the rotating and sliding of particles, and offset the compressive effect of b values. Thus, the contraction of granular materials and the increase of shear strength as the b value increases are significantly restrained. As a result, the inherent anisotropy reduces the effects of stress-induced anisotropy on the mechanical behavior of granular materials.

Data Availability

Some of all data, models, or codes used during the study are available from the corresponding author upon request.

Additional Points

Highlights. (i) The combined effects of inherent and stress-induced anisotropy were studied by DEM. (ii) The oriented granular particles form strong contacts but cause a sliding tendency. (iii) The rotating and sliding of oriented particles are aggravated as b values increase. (iv) Inherent anisotropy reduces the effects of b values on macro-microresponses.

Conflicts of Interest

The authors declare that they have no conflicts of interest.

Acknowledgments

The study was funded by the Fundamental Funds for the Central Universities (22120170129).

References

- [1] Y. Qian, S. J. Lee, E. Tutumluer, Y. M. Hashash, and J. Ghaboussi, "Role of initial particle arrangement in ballast mechanical behavior," *International Journal of Geomechanics*, vol. 18, no. 3, Article ID 04017158, 2018.
- [2] H. Yang, W.-J. Xu, Q.-C. Sun, and Y. Feng, "Study on the meso-structure development in direct shear tests of a granular material," *Powder Technology*, vol. 314, pp. 129–139, 2017.
- [3] J. Zheng and R. D. Hryciw, "Particulate material fabric characterization by rotational haar wavelet transform," *Computers and Geotechnics*, vol. 88, pp. 46–60, 2017.
- [4] M. Mahmud Sazzad, K. Suzuki, and A. Modaresi-Farahmand-Razavi, "Macro-micro responses of granular materials under different b values using DEM," *International Journal of Geomechanics*, vol. 12, no. 3, pp. 220–228, 2012.
- [5] B. Li, L. Chen, and M. Gutierrez, "Influence of the intermediate principal stress and principal stress direction on the mechanical behavior of cohesionless soils using the discrete element method," *Computers and Geotechnics*, vol. 86, pp. 52–66, 2017.
- [6] P. Guo, "Modified direct shear test for anisotropic strength of sand," *Journal of Geotechnical and Geoenvironmental Engineering*, vol. 134, no. 9, pp. 1311–1318, 2008.
- [7] W.-c. Shi, J.-g. Zhu, C.-f. Chiu, and H.-l. Liu, "Strength and deformation behaviour of coarse-grained soil by true triaxial tests," *Journal of Central South University of Technology*, vol. 17, no. 5, pp. 1095–1102, 2010.

- [8] P. V. Lade and J. M. Duncan, "Cubical triaxial tests on cohesionless soil," *Journal of Soil Mechanics & Foundations Div*, vol. 99, no. 10, pp. 793–812, 1973.
- [9] D. A. Sun, W. Huang, and Y. Yao, "An experimental study of failure and softening in sand under three-dimensional stress condition," *Granular Matter*, vol. 10, no. 3, pp. 187–195, 2008.
- [10] P. V. Lade, "Assessment of test data for selection of 3-D failure criterion for sand," *International Journal for Numerical and Analytical Methods in Geomechanics*, vol. 30, no. 4, pp. 307–333, 2006.
- [11] W. Zhou, L. Yang, G. Ma, X. Chang, Y. Cheng, and D. Li, "Macro-micro responses of crushable granular materials in simulated true triaxial tests," *Granular Matter*, vol. 17, no. 4, pp. 497–509, 2015.
- [12] P. V. Lade and M. M. Kirkgaard, "Effects of stress rotation and changes of b -values on cross-anisotropic behavior of natural, K0-consolidated soft clay," *Soils and Foundations*, vol. 40, no. 6, pp. 93–105, 2000.
- [13] P. V. Lade and N. M. Rodriguez, "Comparison of true triaxial and hollow cylinder tests on cross-anisotropic sand specimens," *Geotechnical Testing Journal*, vol. 37, no. 4, pp. 585–596, 2014.
- [14] X. Huang, K. J. Hanley, C. O'Sullivan, C. Y. Kwok, and M. A. Wadee, "DEM analysis of the influence of the intermediate stress ratio on the critical-state behaviour of granular materials," *Granular Matter*, vol. 16, no. 5, pp. 641–655, 2014.
- [15] P. A. Cundall and O. D. L. Strack, "A discrete numerical model for granular assemblies," *Géotechnique*, vol. 29, no. 1, pp. 47–65, 1979.
- [16] H. Huang and E. Tutumluer, "Discrete element modeling for fouled railroad ballast," *Construction and Building Materials*, vol. 25, no. 8, pp. 3306–3312, 2011.
- [17] E. Tutumluer, Y. Qian, Y. M. Hashash, J. Ghaboussi, and D. D. Davis, "Discrete element modelling of ballasted track deformation behaviour," *International Journal of Rail Transportation*, vol. 1, no. 1-2, pp. 57–73, 2013.
- [18] T.-T. Ng, "Macro- and micro-behaviors of granular materials under different sample preparation methods and stress paths," *International Journal of Solids and Structures*, vol. 41, no. 21, pp. 5871–5884, 2004.
- [19] M. M. Sazzad and K. Suzuki, "Micromechanical behavior of granular materials with inherent anisotropy under cyclic loading using 2D DEM," *Granular Matter*, vol. 12, no. 6, pp. 597–605, 2010.
- [20] O. I. Imole, M. Wojtkowski, V. Magnanimo, and S. Luding, "Micro-macro correlations and anisotropy in granular assemblies under uniaxial loading and unloading," *Physical Review E*, vol. 89, no. 4, Article ID 042210, 2014.
- [21] E. S. Hosseininia, "Investigating the micromechanical evolutions within inherently anisotropic granular materials using discrete element method," *Granular Matter*, vol. 14, no. 4, pp. 483–503, 2012.
- [22] D. Barreto and C. O'Sullivan, "The influence of inter-particle friction and the intermediate stress ratio on soil response under generalised stress conditions," *Granular Matter*, vol. 14, no. 4, pp. 505–521, 2012.
- [23] M. R. Kuhn, W. Sun, and Q. Wang, "Stress-induced anisotropy in granular materials: fabric, stiffness, and permeability," *Acta Geotechnica*, vol. 10, no. 4, pp. 399–419, 2015.
- [24] T.-T. Ng, "Shear strength and micro-descriptors of bidisperse ellipsoids under different loading paths," *Mechanics of Materials*, vol. 41, no. 6, pp. 748–763, 2009.
- [25] S. Lobo-Guerrero and L. E. Vallejo, "Discrete element method analysis of railroad ballast degradation during cyclic loading," *Granular Matter*, vol. 8, no. 3-4, pp. 195–204, 2006.
- [26] H. A. Carmona, A. V. Guimarães, J. S. Andrade Jr., I. Nikolakopoulos, F. K. Wittel, and H. J. Herrmann, "Fragmentation processes in two-phase materials," *Physical Review E*, vol. 91, no. 1, Article ID 012402, 2015.
- [27] Z. Tong, P. Fu, S. Zhou, and Y. F. Dafalias, "Experimental investigation of shear strength of sands with inherent fabric anisotropy," *Acta Geotechnica*, vol. 9, no. 2, pp. 257–275, 2014.
- [28] W. J. Xu, G. Y. Liu, and H. Yang, "Study on the mechanical behavior of sands using 3D discrete element method with realistic particle models," *Acta Geotechnica*, vol. 15, no. 10, pp. 2813–2828, 2020.
- [29] Z. Mahmood and K. Iwashita, "Influence of inherent anisotropy on mechanical behavior of granular materials based on DEM simulations," *International Journal for Numerical and Analytical Methods in Geomechanics*, vol. 34, no. 8, pp. 795–819, 2010.
- [30] H. Boler, Y. Qian, and E. Tutumluer, "Influence of size and shape properties of railroad ballast on aggregate packing: statistical analysis," *Transportation Research Record: Journal of the Transportation Research Board*, vol. 2448, no. 1, pp. 94–104, 2014.
- [31] Y. Xiao, E. Tutumluer, and Y. Qian, "DEM approach for engineering aggregate gradation and shape properties influencing mechanical behavior of unbound aggregate materials," in *Geo-Congress 2014: Geo-Characterization and Modeling for Sustainability*, pp. 2898–2910, Reston, VA, USA, 2014.
- [32] X. Lin and T.-T. Ng, "A three-dimensional discrete element model using arrays of ellipsoids," *Géotechnique*, vol. 47, no. 2, pp. 319–329, 1997.
- [33] P. Fu and Y. F. Dafalias, "Study of anisotropic shear strength of granular materials using DEM simulation," *International Journal for Numerical and Analytical Methods in Geomechanics*, vol. 35, no. 10, pp. 1098–1126, 2011.
- [34] A. A. Mirghasemi, L. Rothenburg, and E. L. Matyas, "Influence of particle shape on engineering properties of assemblies of two-dimensional polygon-shaped particles," *Géotechnique*, vol. 52, no. 3, pp. 209–217, 2002.
- [35] A. A. Peña, A. Lizcano, F. Alonso-Marroquin, and H. J. Herrmann, "Biaxial test simulations using a packing of polygonal particles," *International Journal for Numerical and Analytical Methods in Geomechanics*, vol. 32, no. 2, pp. 143–160, 2008.
- [36] R. Taghavi, "Automatic clump generation based on mid-surface," in *Proceedings of the 2nd International FLAC/DEM Symposium*, pp. 791–797, Melbourne, Australia, February 2011.
- [37] X. Bian, H. Huang, E. Tutumluer, and Y. Gao, "Critical particle size" and ballast gradation studied by discrete element modeling," *Transportation Geotechnics*, vol. 6, pp. 38–44, 2016.
- [38] B. S. Kim, S. W. Park, and S. Kato, "DEM simulation of collapse behaviours of unsaturated granular materials under general stress states," *Computers and Geotechnics*, vol. 42, pp. 52–61, 2012.
- [39] X. Gu, M. Huang, and J. Qian, "DEM investigation on the evolution of microstructure in granular soils under shearing," *Granular Matter*, vol. 16, no. 1, pp. 91–106, 2014.
- [40] N. H. Minh and Y. P. Cheng, "A DEM investigation of the effect of particle-size distribution on one-dimensional compression," *Géotechnique*, vol. 63, no. 1, pp. 44–53, 2013.

- [41] JGS, *Japanese Standards and Explanations of Laboratory Tests of Geomaterials*, vol. 1, Japanese Geotechnical Society, Tokyo, Japan, 2010.
- [42] B. Dai, J. Yang, and X. Luo, "A numerical analysis of the shear behavior of granular soil with fines," *Particuology*, vol. 21, pp. 160–172, 2015.
- [43] B. Dai, J. Yang, C. Zhou, and X. Luo, "DEM investigation on the effect of sample preparation on the shear behavior of granular soil," *Particuology*, vol. 25, pp. 111–121, 2016.
- [44] Itasca Consulting Group, Inc., *Particle Flow Code in 3 Dimensions (PFC3D) Version 4*, vol. 3, Itasca Consulting Group, Inc., Minneapolis, MN, USA, 2008.
- [45] C. Goldenberg and I. Goldhirsch, "Friction enhances elasticity in granular solids," *Nature*, vol. 435, no. 7039, pp. 188–191, 2005.
- [46] W. M. Yan and J. Dong, "Effect of particle grading on the response of an idealized granular assemblage," *International Journal of Geomechanics*, vol. 11, no. 4, pp. 276–285, 2011.
- [47] J. E. Andrade, Q. Chen, P. H. Le, C. F. Avila, and T. Matthew Evans, "On the rheology of dilative granular media: bridging solid- and fluid-like behavior," *Journal of the Mechanics and Physics of Solids*, vol. 60, no. 6, pp. 1122–1136, 2012.
- [48] Shi W., True triaxial tests on coarse-grained soils and study on constitutive model, Dissertation for the doctoral degree, Hohai University, Nanjing, China, 2008, in Chinese.
- [49] N. Guo and J. Zhao, "The signature of shear-induced anisotropy in granular media," *Computers and Geotechnics*, vol. 47, pp. 1–15, 2013.
- [50] M. U. Ergun, "Evaluation of three-dimensional shear testing," in *Proceedings of the 10th International Conference on Soil Mechanics and Foundation Engineering*, vol. 1, pp. 593–596, Stockholm, Sweden, June 1981.
- [51] J. Zhao and N. Guo, "Rotational resistance and shear-induced anisotropy in granular media," *Acta Mechanica Solida Sinica*, vol. 27, no. 1, pp. 1–14, 2014.
- [52] S. Nemat-Nasser and Y. Tobita, "Influence of fabric on liquefaction and densification potential of cohesionless sand," *Mechanics of Materials*, vol. 1, no. 1, pp. 43–62, 1982.
- [53] F. Alonso-Marroquin, S. Luding, H. J. Herrmann, and I. Vardoulakis, "Role of anisotropy in the elastoplastic response of a polygonal packing," *Physical Review E*, vol. 71, no. 5, Article ID 051304, 2005.
- [54] S. Yimsiri and K. Soga, "DEM analysis of soil fabric effects on behaviour of sand," *Géotechnique*, vol. 60, no. 6, pp. 483–495, 2010.
- [55] Y. Liu, D. Zhang, S. Wu, and P. Yu, "DEM Investigation on the evolution of fabric under true triaxial conditions in granular materials," *International Journal of Geomechanics*, vol. 20, no. 8, Article ID 04020110, 2020.
- [56] L. Rothenburg and R. J. Bathurst, "Analytical study of induced anisotropy in idealized granular materials," *Géotechnique*, vol. 39, no. 4, pp. 601–614, 1989.
- [57] T. G. Sitharam, S. V. Dinesh, and N. Shimizu, "Micro-mechanical modelling of monotonic drained and undrained shear behaviour of granular media using three-dimensional DEM," *International Journal for Numerical and Analytical Methods in Geomechanics*, vol. 26, no. 12, pp. 1167–1189, 2002.
- [58] H. Ouadfel and L. Rothenburg, "'Stress-force-fabric' relationship for assemblies of ellipsoids," *Mechanics of Materials*, vol. 33, no. 4, pp. 201–221, 2001.
- [59] A. Tordesillas, J. Zhang, and R. Behringer, "Buckling force chains in dense granular assemblies: physical and numerical experiments," *Geomechanics and Geoengineering*, vol. 4, no. 1, pp. 3–16, 2009.
- [60] J. Liu, W. Zhou, G. Ma, S. Yang, and X. Chang, "Strong contacts, connectivity and fabric anisotropy in granular materials: a 3D perspective," *Powder Technology*, vol. 366, pp. 747–760, 2020.